Unsteady disturbances in a swept wing boundary layer due to plasma forcing

Physics of Fluids

Unsteady disturbances in a swept wing boundary layer due to plasma forcing

Cite as: Phys. Fluids **34**, 114115 (2022); https://doi.org/10.1063/5.0124818
Submitted: 08 September 2022 • Accepted: 20 October 2022 • Published Online: 08 November 2022
Published open access through an agreement with Technische Universiteit Delft Faculteit Luchtvaart- en Ruimtevaarttechniek

K. Peng (彭开晟), F. Avallone and M. Kotsonis

Physics of Fluids ARTICLE scitation.org/journal/phf

Unsteady disturbances in a swept wing boundary layer due to plasma forcing

Cite as: Phys. Fluids **34**, 114115 (2022); doi: 10.1063/5.0124818
Submitted: 8 September 2022 · Accepted: 20 October 2022 ·
Published Online: 8 November 2022

K. Peng (彭开晟),[a] F. Avallone, and M. Kotsonis

AFFILIATIONS

FPT Department, Faculty of Aerospace Engineering, Delft University of Technology, Kluyverweg 1, Delft 2629HS, The Netherlands

[a]Author to whom correspondence should be addressed: K.Peng@tudelft.nl

ABSTRACT

This work investigates the response of a transitional boundary layer to spanwise-invariant dielectric barrier discharge plasma actuator (PA) forcing on a 45° swept wing at a chord Reynolds number of 2.17×10^6. Two important parameters of the PA operation are scrutinized, namely, the forcing frequency and the streamwise location of forcing. An array of passive discrete roughness elements is installed near the leading edge to promote and condition a set of critical stationary crossflow (CF) instability modes. Numerical solutions of the boundary layer equations and linear stability theory are used in combination with the experimental pressure distribution to provide predictions of critical stationary and traveling CF instabilities. The laminar–turbulent transition front is visualized and quantified by means of infrared thermography. Measurements of velocity fields are performed using hotwire anemometry scans at specific chordwise locations. The results demonstrate the inherent introduction of unsteady velocity disturbances by the plasma forcing. It is shown that, depending on actuator frequency and location, these disturbances can evolve into typical CF instabilities. Positive traveling low-frequency type III modes are generally amplified by PA in all tested cases, while the occurrence of negative traveling high-frequency type I secondary modes is favored when PA is operating at high frequency and at relatively downstream locations, with respect to the leading edge.

I. INTRODUCTION

Swept wings of modern aircraft are characterized by the development of a three-dimensional boundary layer, inside which the so-called crossflow (CF) velocity component arises due to the imbalance between the centripetal and pressure forces. The CF component is perpendicular to the outer inviscid streamline, which results in an inflectional velocity shape thus giving rise to the so-called CF instabilities. Depending on the environmental conditions (i.e., surface roughness and freestream turbulence intensity T_u), a combination of stationary and traveling CF instabilities are amplified and eventually cause laminar–turbulent transition.[1] In realistic cruise conditions where T_u is low, stationary CF instabilities prevail and develop in the form of spatially fixed co-rotating vortices, which modulate the boundary layer, resulting in pronounced wall-normal and spanwise shears. These pronounced shears support the development of unsteady secondary instabilities, which ultimately drive the laminar–turbulent transition process.[2] Comprehensive and detailed reviews on the topic are given by Refs. 3–5.

The dominant role of CF instabilities in the swept wing boundary layer exposes the necessity of controlling them with the eventual goal of transition delay. A range of relevant control strategies are proposed and investigated, which are reviewed by Refs. 6–8. One promising strategy involves the use of the so-called discrete roughness elements (DRE) and was first proposed by Saric *et al.*[9] and later generalized as upstream flow deformation (UFD) by Wasserman and Kloker.[10] According to the DRE/UFD technique, sub-critical stationary CF instabilities, which feature smaller wavelength than the most amplified stationary mode (i.e., the critical mode), are forced near the leading edge. These sub-critical modes are in general less unstable than the critical mode. As a result of non-linear interactions, the enhanced sub-critical modes suppress the onset and destabilization of the critical mode thus delaying transition. Though considerable studies have demonstrated the efficacy of the DRE/UFD technique,[4,11] successful transition delay by this technique is only limitedly reported in the experiment, while proven challenging to repeat in flight testing.[12] This could be attributed to the high sensitivity of the DRE/UFD strategy to external factors such as DRE shape quality, freestream turbulence intensity, and boundary layer characteristics.[13,14] This sensitivity exposes the need for active control methods as purely passive ones can be less effective or even detrimental in off-design or changing conditions.

As a promising family of active flow control techniques, dielectric barrier discharge (DBD) plasma actuators (PAs) have recently gained

attention due to their inherent capability of manipulating boundary layer instabilities. This active control device poses particular features including low power consumption, fast response, and fully electronic operation without moving parts. PA working principles and characterization studies are summarized by Refs. 15–17. Specifically targeting laminar–turbulent boundary layer transition, PA-based control approaches have been mostly applied to 2D unswept boundary layers (e.g., the cancelation of Tollmien–Schlichting waves as shown by Refs. 18–20), while attempts on the swept wing boundary layer began more recently, as reviewed below.

Several PA-based strategies have been proposed to mitigate the CF component and CF instabilities, namely, the so-called DRE/UFD, direct attenuation, and base flow modification (BFM) strategies. In brief, the UFD strategy leverages discrete/localized PA forcing to amplify sub-critical stationary CF modes thus suppressing the critical stationary modes' growth, as demonstrated by Dörr and Kloker.[21] On the other hand, the direct attenuation strategy utilizes the PA forcing to locally oppose the rotation of stationary CF vortices, as demonstrated by Dörr and Kloker.[22] In contrast, the BFM strategy aims at directly reducing the source of CF instabilities, namely, the CF component in the boundary layer. The reduction of CF component results in overall boundary layer stabilization and thus reduced amplification of both stationary and traveling CF instabilities, eventually yielding the transition delay, which is numerically validated by Dörr and Kloker[23] and experimentally demonstrated by Yadala *et al.*[24] While the use of PAs for swept wing transition delay has been proposed in several variations, several challenges remain in their actual implementation. One of the largely unknown factors influencing the PA efficacy is the introduction of non-deterministic unsteady flow disturbances, inherently contained in the discharge formation. In numerical simulation work, the PA discharge unsteadiness is usually neglected or simplified as a purely harmonic component featuring the actuation frequency f_{AC}. Conversely, recent experimental observations[8,25–27] found enhanced velocity disturbances within a broad frequency range (though centralized at f_{AC}).

By means of linear stability theory (LST) and a simplified body force model, Serpieri[8] attributed the unsteady disturbances to the inherent unsteadiness of the PA forcing, possibly related to the stochastic dynamics of the electrical discharge. This assumption was later confirmed by Moralev *et al.*[25] Using the cross-spectra analysis, they traced the origin of the random unsteady disturbances to the quasi-stochastic nature of PA micro-discharges. Considering that the micro-discharge formation is an inherent feature of typical DBD PAs, the effects of these unavoidable disturbances on the boundary layer require further investigation. This becomes particularly pertinent when the frequency of these stochastic disturbances overlaps with those of the most amplified traveling CF instabilities. Furthermore, these amplified unsteady disturbances could quadratically/non-linearly interact with stationary CF instabilities, resulting in the rapid spectral broadening of the perturbation system and eventual transition to turbulence, as found by Corke *et al.*[28] and Arndt *et al.*[29] In summary, the successful deployment of PA-based control for swept wing transition necessitates the elucidation of the origin and growth mechanisms of these unsteady disturbances, as well as their dependence on pertinent forcing parameters such as frequency and location.

The present study is aimed at the measurement of unsteady PA-induced perturbations in a swept wing boundary layer dominated by stationary CF vortices, representative of typical cruise flight regimes. According to previous numerical studies of Refs. 10 and 30, the frequency and the origin location of unsteady disturbances have pronounced effects on the development of CF instabilities. As such, two corresponding parameters of PA operation are investigated in this work, namely, the applied voltage frequency f_{AC} and the forcing location. The choice of these parameters is directly related to the operation of the actuator and the stability characteristics of the flow. The unsteady dynamics within the plasma discharge formation inherently depend on the applied voltage frequency f_{AC}.[25] On the other hand, the receptivity, growth, and topology of primary and secondary unsteady CF instabilities are known to be highly dependent on the primary CF stationary vortex development, which in turn is related to the given streamwise location of their interaction.[5]

It should be emphasized here that the current study is aimed at investigating the PA-induced unsteady disturbances instead of delaying transition. As such, PAs are operated at lower power and lower f_{AC} compared to previous studies reporting transition delay (Yadala *et al.*,[24] $f_{AC} = 10$ kHz), thus minimizing the BFM effect and mainly investigating the unsteady effects. This paper is organized in the following order: Section II provides a description of the experimental setup, measurement techniques, and a preliminary prediction of the expected instabilities using linear stability theory. Sections III and IV report infrared (IR) imaging and hotwire measurement results and corresponding analysis. Finally, the conclusions of this study are summarized in Sec. V.

II. EXPERIMENTAL SETUP AND METHODOLOGY

A. Wind tunnel facility and swept wing model

The experiment was conducted in the low turbulence tunnel (LTT) located at TU Delft. This closed-loop subsonic tunnel features a sufficiently low turbulence intensity ($T_u/U_\infty = 0.07\%$ at the freestream velocity of 24 m/s) for creating a transition scenario dominated by stationary CF instabilities.[31] The employed wind tunnel model is an in-house designed 45° swept wing model 66018*M3J*, which is fully described by Serpieri and Kotsonis.[32] The wing model has an unswept chord (in x direction) of $c_x = 0.9$ m and can approximate infinite swept wing conditions when placed at appropriate angles of attack. The wing model geometry is given in Fig. 1(a). The small leading-edge radius and a continuously favorable pressure gradient (up to $x/c_x = 0.65$) guarantee a boundary layer dominated by CF instabilities. For the present experiment, the model is placed at angle of attack $\alpha = 3.3°$ and the pressure side is investigated. The pressure coefficient C_p as shown in Fig. 1(a) is measured at Reynolds number $Re_X = 2.17 \times 10^6$ (based on swept chord $c_X = 1.27$ m), corresponding to freestream velocity of $U_\infty = 25.5$ m/s. A minimal difference between the top and bottom pressure coefficient confirms the attainment of spanwise invariant conditions. For the remainder of this work, two coordinate reference systems are used. The first is aligned with the wind tunnel and denoted as *XYZ*, while the second is body-fitted to the swept wing model and denoted as *xyz*, where y is aligned normal to the local surface of the wing, as shown in Fig. 1(b). The corresponding velocity vectors are represented by $[U\ V\ W]$ and $[u\ v\ w]$, respectively.

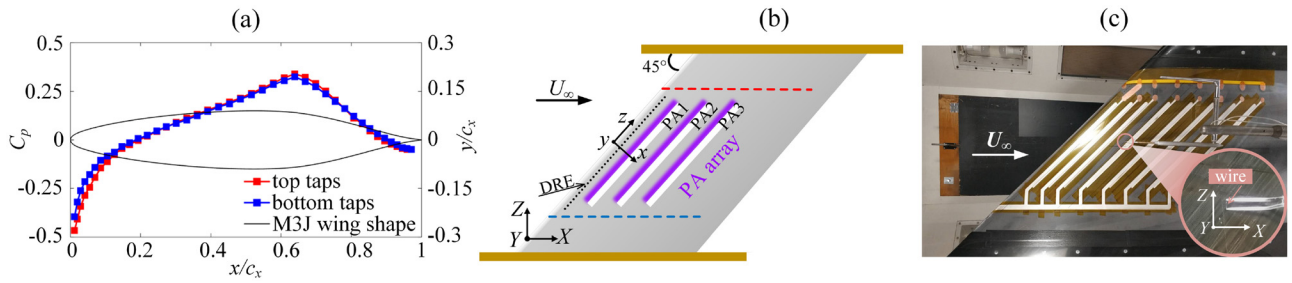

FIG. 1. (a) Cross section of *M3J* (in *x* direction) and experimental pressure coefficient C_p at $\alpha = 3.3°$ and $\mathrm{Re}_X = 2.17 \times 10^6$; (b) diagram of *M3J* with PA arrays. Two coordinate systems are given aligned with the wind tunnel *XYZ* and the swept wing model *xyz*. Red and blue dashed lines illustrate locations of top and bottom pressure taps; (c) photograph of experimental model (note that more plasma actuator arrays are visible than used in the present work).

B. Plasma actuator and discrete roughness elements

The primary goal of the present study is to elucidate the effects of PA-induced unsteady perturbations on a swept wing boundary layer dominated by stationary CF instabilities, in the framework of the BFM strategy. An essential requirement for such flow is the existence and development of stationary CF vortices, which serve as the target of this flow control technique. For the present experiments, the critical stationary CF mode (predicted by linear stability theory presented in Sec. II E) is forced using a DRE array installed on the wing surface at $x/c_x = 0.02$ with a spanwise spacing of $\lambda_{\mathrm{DRE}} = 8$ mm. The DRE array is scanned through a scanCONTROL 30xx profilometer operating with a semiconductor laser, which has a wavelength of 405 nm and reference resolution of 1.5 μm.[33] The scanning results show that the DRE array features an average height of $h_{\mathrm{DRE}} = 0.1147 \pm 0.0023$ mm and a diameter of $d_{\mathrm{DRE}} = 1.772 \pm 0.017$ mm, which effectively triggers the critical stationary CF vortices, as confirmed by previous experiments at similar conditions.[33,34]

For the actuation, an array of 2D spanwise-invariant DBD plasma actuators is utilized, similar to the configuration used by Yadala *et al.*[24] for BFM control. Following the same fabrication technique, the PA electrodes are constructed using computer-controlled spray-on conductive silver paint. The width of exposed and grounded electrodes is 5 and 10 mm, respectively, as shown in Fig. 2. Following the BFM control principle, the PA is placed near the leading edge and oriented to force in the $-x$ direction. To investigate the influence of the PA streamwise location, three spanwise-invariant actuators are printed and positioned at locations of $x/c_x = 0.035$, 0.073, and 0.11, respectively. A sheet of 500-μm-thick polyethylene terephthalate (PET) foil is used as the dielectric material. In order to form a smooth wing surface and avoid geometrical irregularities, the PET foil is made large enough to wrap around the leading edge and extend downstream until the trailing edge. The three PAs are henceforth referred to as PA1, PA2, and PA3, respectively. A Trek 20/20C HS high-speed high-voltage amplifier is used as the power supply, delivering a sinusoidal high-voltage signal at selected combinations of amplitudes (V_{p-p}) and frequencies (f_{AC}). During the experiment, the three actuators are powered individually, with only one actuator active per time.

C. Infrared thermography

Following Reynolds' analogy, high shear flow can be expected to enhance convective heat transfer with respect to low shear flow. If the aerodynamic surface is actively (i.e., externally) heated, the difference in heat convection rate through the surface skin can be translated into a difference in surface temperature. Therefore, infrared (IR) thermography can be used to retrieve the stationary CF vortex footprint and the laminar–turbulent transition front, owing to their large impact on the local shear at the wall. In the present experiment, an Optris PI640 IR camera (640 × 480 px, NETID 75 mK) is mounted outside of the wind tunnel test section and measures the wing model surface temperature. It should be stressed that the IR camera is not thermally calibrated as the IR images are used only for flow visualization. To enhance the thermal contrast, the wing model is radiated by several halogen lamps. The camera acquires at 4 Hz and approximately 80 IR images are recorded per case, which are later averaged in order to minimize the background noise.

The transition front identification used here follows the differential infrared thermography (DIT) approach as shown by Raffel *et al.*[35] Specifically, at each testing configuration (i.e., PA location and frequency), IR recordings are taken at two Reynolds numbers (i.e., the nominal $\mathrm{Re}_X = 2.17 \times 10^6$ and the higher $\mathrm{Re}_X = 2.7 \times 10^6$), by varying the wind tunnel freestream velocity. The resulting two average temperature distributions are mutually subtracted to obtain a

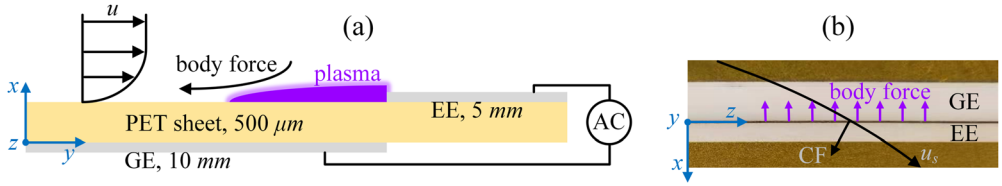

FIG. 2. (a) Schematic of PA in the *xy* plane. (b) Top view (photograph) of the PA and forcing arrangement (*xz* plane). EE: exposed electrode; GE: grounded electrode; u_s: streamline aligned velocity; CF: crossflow component.

differential image. As such, the image quality is improved by minimizing the background noise, reflections, and non-uniformities, retaining only the relative change in temperature between the two Reynolds number conditions. Finally, the transition front is identified based on the spatial gradient maxima of the differential image. A linear fitting is performed to quantify the transition location, corresponding to the nominal Reynolds number condition. A full description of the preprocessing and details of this procedure are given by Rius-Vidales *et al.*[36]

D. Hotwire anemometry

Hotwire anemometry (HWA) is utilized to quantify the unsteady behavior of the flow due to PA forcing. The measurements are carried out using a single-wire boundary layer probe (Dantec Dynamics P15) operated by a TSI IFA-300 constant temperature anemometer bridge with automatic adjustment of overheat ratio.[8] The hotwire is calibrated *in situ* daily and appropriate corrections are applied for small changes in freestream temperature and barometric pressure during the experiment. The hotwire signals for each measurement point are recorded for a period of 2 s and digitized using an analog/digital 24-bit converter at a sampling rate of 51.2 kHz. Due to the deterministic operation of PAs, the induced flow perturbations are expected to be phase conditioned to the forcing signal.[37] In order to perform phase-resolved analysis, the high-voltage and current signals delivered to the PA are acquired in synchronization to the hotwire velocity signal.

To monitor the developing boundary layer, the hotwire scans are conducted at two fixed chordwise locations, namely, $x/c_x = 0.15$ and 0.2. The hotwire scans are adjusted to be normal to the local wing surface (i.e., the yz plane). Each scanning plane encompasses 30×32 points in y and z axes, respectively, and features a spanwise spacing resolution of $d_z = 0.5$ mm. The wall-normal spacing resolution is set as $d_y = 0.0667$ mm for $x/c_x = 0.15$ and $d_y = 0.0733$ mm for $x/c_x = 0.2$. The hotwire scan locations are automatically set using an automated traverse system (installed in the wind tunnel diffuser) with a step resolution of 2.5 μm in all three axes of translation.[8] The wire is aligned with the Z axis [Fig. 1(c)], thus measuring the Euclidean sum of velocity components along the X and Y axes [i.e., $|U_{HW}| = (U^2 + V^2)^{1/2}$].[31] In this work, overbar symbols denote non-dimensional quantities. Specifically, the velocity components are non-dimensionalized by the total freestream velocity $U_\infty = 25.5$ m/s with z non-dimensionalized as $\bar{z} = z/\lambda_{\mathrm{DRE}}$. In addition, y is non-dimensionalized as $\bar{y} = y/\delta_0$, where δ_0 is the Blasius length scale as described in Sec. II E.

E. Linear stability theory

In low freestream turbulence conditions, the critical stationary CF modes are eventually responsible for transition, through the development of secondary instabilities. Nevertheless, an operated PA will inherently produce stochastic disturbances, which can potentially amplify the most unstable traveling CF instabilities, leading to the non-linear interaction with stationary CF instabilities.[25] The potential non-linear interaction between these primary CF instabilities can be responsible for the spectral broadening of the disturbance system, thus accelerating laminar breakdown.[29,38] Notwithstanding the eventual non-linear interactions, the initial linear growth of these CF instabilities can be predicted by linear stability theory (LST). As such, LST is used to gain a preliminary prediction of the behavior of stationary and traveling CF instabilities at the tested conditions. Prior to the LST analysis, the mean flow profiles of the baseline boundary layer are calculated based on the experimental pressure distribution of the wind tunnel model [Fig. 1(a)]. Assuming spanwise invariant conditions, the 3D incompressible boundary layer equations are simplified to a 2.5D formulation by decoupling the z-momentum equations. The solutions of the stability problem are obtained by solving the Orr–Sommerfeld equation with various combinations of angular frequency ω and spanwise wavenumber β. Finally, the integral amplification N factor ($N = \int_0^s -\alpha_i \, \mathrm{ds}$) is calculated where $-\alpha_i$ is the streamwise growth rate and s is the surface distance starting from the attachment line. In this paper, the Blasius length scale $\delta_0 = \nu s_0/u_0 = 3.48 \times 10^{-4}$ m is used as the reference length. Specifically, ν is the kinematic viscosity, $s_0 = 0.138$ m is the surface distance from the attachment line to $x/c_x = 0.15$, and $u_0 = 16.65$ m/s is the edge velocity at $x/c_x = 0.15$. A description of linear stability theory and term definitions can be found in the work of Mack.[39]

Figure 3(b) shows the non-dimensional streamwise growth rate $-\bar{\alpha}_i = -\alpha_i \delta_0$ and N factor of stationary modes. Despite the earlier growth of smaller wavelength modes, the mode of $\lambda = 8$ mm emerges as most integrally amplified in the considered domain, in agreement with previous studies at similar conditions.[8,24] Figures 3(c)–3(h) illustrate N factors of traveling modes of $f = 100$, 200, and 300 Hz. Essentially, traveling CF instabilities consist of two distinct wave families propagating in opposite directions, namely, the positive and negative traveling modes. Generally, positive modes travel against the CF direction, while the negative modes travel along the CF direction.[2,40] Figure 3(a) depicts the directions of positive and negative traveling modes in the yz plane (looking from upstream). The LST results illustrate that negative traveling modes are significantly amplified at $f < 100$ Hz, while positive traveling modes are most amplified around $f = 200$ Hz. In fact, positive traveling modes are completely suppressed once f surpasses 1000 Hz (not shown here). Compared with positive traveling modes, negative traveling modes are evidently weaker (more evident at higher frequencies), which agrees with the observation of Guo and Kloker.[2] The apparent stabilization of both directional modes at high frequencies indicates that PAs should be actuated at high f_{AC} to avoid directly introducing traveling CF instabilities of low frequencies. Additionally, the current results indicate that low-frequency positive traveling modes are expected to play a more important role in the transition dynamics compared with their negative counterparts due to their relatively higher amplification.

III. PA EFFECT ON TRANSITION TOPOLOGY AND LOCATION

In this section, the effects of f_{AC} and PA location on the topology and location of laminar–turbulent transition are parametrically investigated by means of IR thermography. Due to the external radiation from the halogen lamps, the laminar flow region features a higher temperature than turbulent flow in IR images. The PA electrodes appear as dark strips of lower temperature due to their low emissivity.

The surface temperature topology for PA1 is visualized by the time-averaged IR field and illustrated in Fig. 4. Qualitatively similar topology is found for the other two PA cases (not shown here for brevity). In addition, to investigate PA effects on stationary CF vortices, a spatial fast Fourier transform (FFT) is applied on the time-averaged IR field in the spanwise direction. The spectral results are illustrated in

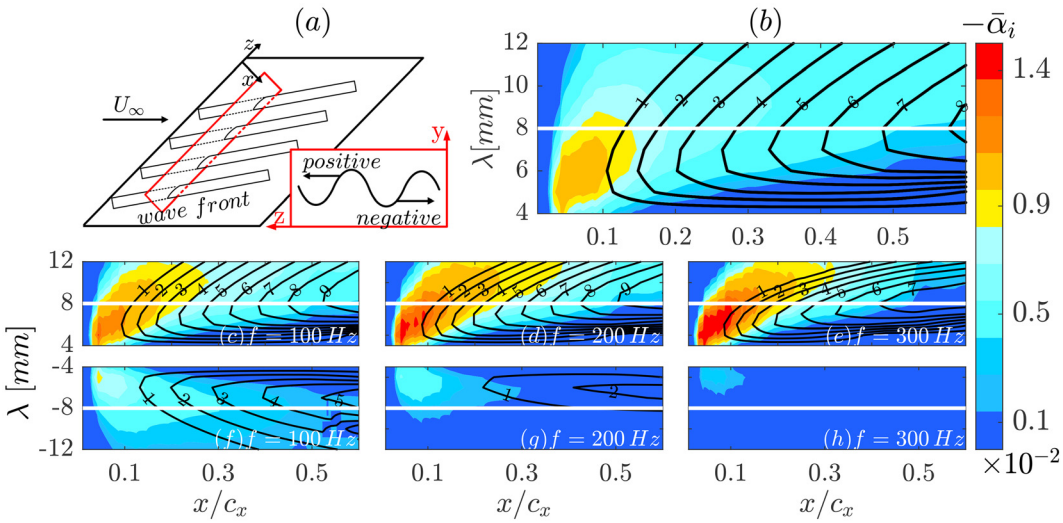

FIG. 3. (a) Schematic of positive and negative traveling CF instabilities. Inset depicts the traveling mode's direction in the *yz* plane (looking from upstream); non-dimensional growth rate in x/c_x ($-\bar{\alpha}_i$, colored) and corresponding *N* factors (black iso-lines) of (b) stationary CF instabilities ($f = 0$ Hz); (c)–(e) positive traveling CF modes; (f)–(h) negative traveling modes. The white line indicates the wavelength λ of ± 8 mm.

plots next to the IR fields, corresponding to the region outlined by the magenta box. The abscissa of the spectra is x/c_x (from 0.12 to 0.16) and the ordinate is the non-dimensional wavenumber $\bar{\gamma} = 1/\bar{\lambda}$, with resolution $\Delta\bar{\gamma} = 0.0349$. The wavenumber $\bar{\gamma} = 1$ corresponds to the critical stationary mode of $\lambda = 8$ mm. In the PA-off case, the typical jagged transition front occurs around $x/c_x = 0.4$, demonstrating the dominance of stationary CF instabilities in the boundary layer. As expected, an evident spectral peak is found at $\bar{\gamma} = 1$, further confirming the conditioning of critical stationary vortices, which result from the upstream DRE excitation.

The operation of PA1 exerts a significant alteration on the transition front. Compared with the PA-off case, the transition front evidently moves upstream and becomes spatially blurred, losing the distinct jagged pattern. This effect is more pronounced for low-frequency plasma excitation at $f_{AC} = 200$, 300, and 500 Hz. The corresponding wavenumber spectra quantitatively demonstrate the topological observations as the $\bar{\gamma} = 1$ signature is significantly weaker for these cases. The change in transition topology offers a first indication of the transitional scenario alteration due to the enhanced traveling CF instabilities by the PA, as these are known to decrease the spatial coherence of the transition front.[8] Compared with low f_{AC} forcing, the high $f_{AC} = 3000$ Hz forcing appears to have a milder effect on the transition. At this condition, the transition front is located further downstream and is less blurred, indicating that traveling CF instabilities are less dominant [also demonstrated by the pronounced spectral peak at $\bar{\gamma} = 1$ in Fig. 4(f)]. The current observation agrees well with the reported LST predictions, in which high-frequency traveling CF instabilities are found to be linearly stable in the present flow.

The transition location is quantified by evaluating the time-averaged IR images following the method described by Rius-Vidales

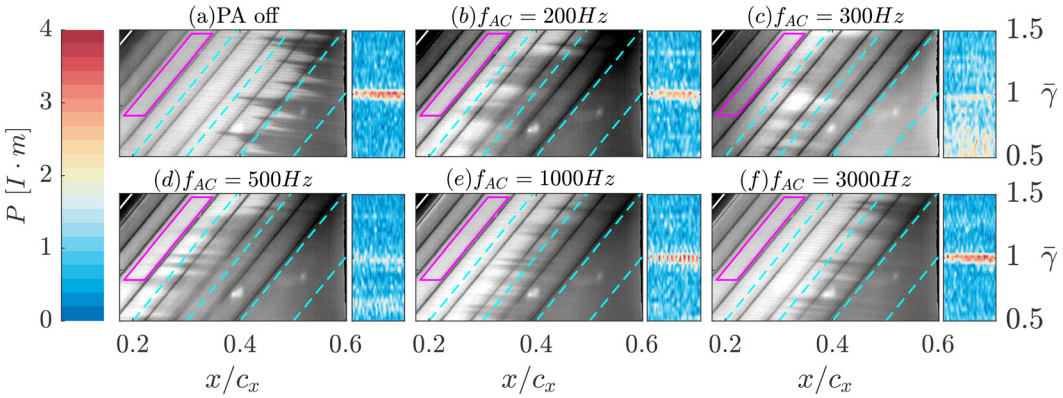

FIG. 4. Time-averaged IR imaging, where PA1 works with $V_{p-p} = 10$ kV at (a) $f_{AC} = 0$ Hz (PA-off); (b) $f_{AC} = 200$ Hz; (c) $f_{AC} = 300$ Hz; (d) $f_{AC} = 500$ Hz; (e) $f_{AC} = 1000$ Hz; (f) $f_{AC} = 3000$ Hz. The flow comes from left, and the leading edge is shown by the white line in the upper-left corner. The wavenumber spectra correspond to IR domain outlined by magenta lines. Cyan dashed lines denote constant chord positions.

et al.[36] To quantify the PA effects, the transition shift $\Delta(x_t/c_x)$ is calculated as below

$$\Delta(x_t/c_x) = (x_t/c_x)_{\text{off}} - (x_t/c_x)_{\text{on}}, \quad (1)$$

where x_t/c_x is the transition location and the subscript indicates the PA working condition (i.e., on or off). The transition shift $\Delta(x_t/c_x)$ at $V_{p-p} = 10$ kV for various f_{AC} is summarized in Fig. 5. Overall, a positive transition shift $\Delta(x_t/c_x)$ is observed for all cases, indicating that transition moves upstream due to the PA operation. Furthermore, in the low-frequency range of $f_{AC} < 800$ Hz, PA1 appears to have the most evident promoting effect on transition shift $\Delta(x_t/c_x)$, in comparison with PA2 and PA3. Considering PA1 is located closer to the leading edge, it can be expected that induced low-frequency disturbances will experience a longer chordwise amplification and result in stronger accumulated amplitudes compared with those in PA2 and PA3 cases.[37] However, by increasing f_{AC} to higher values, the transition shift $\Delta(x_t/c_x)$ of PA1 decays rapidly, indicating the limited enhancing effects of PA1 on high-frequency disturbances. In fact, the high f_{AC} operation is expected to impart more energy into the boundary layer, as the plasma-generated body force magnitude is increasing with f_{AC}.[15] Consequently, the PA-induced velocity disturbances at high frequencies are expected to have larger initial amplitudes than in the case of low-frequency forcing. Still, the transition shift $\Delta(x_t/c_x)$ at low f_{AC} operation surpasses that of high f_{AC} forcing, demonstrating that low-frequency unsteady disturbances are more dominant than high-frequency instabilities. On the other hand, a significantly weaker effect on the transition shift $\Delta(x_t/c_x)$ is found for PA2 and PA3 when operated at low f_{AC}. Instead, the operation of the two downstream PAs has an increasingly strong effect on the transition location with increasing f_{AC}.

The overall transition advancement reported in the present study further highlights the detrimental effects of PA-induced unsteady disturbances and partially resolves the conundrum regarding the effects of unsteady forcing within the context of the BFM method. In the work of Peng *et al.*,[41] the BFM-based PA was found to essentially impose two effects into the boundary layer. One is to weaken stationary CF instabilities (i.e., the intended BFM action), while the other is to enhance unsteady instabilities. Nonetheless, the effects of these amplified unsteady instabilities remain unknown. Guo and Kloker[2] have shown that forced unsteady CF instabilities can possibly delay transition (through weakening stationary CF instabilities by interaction), while on the other hand, they tend to promote transition due to their significant growth rates. The current results, where transition is promoted with all tested f_{AC}, indicate that unsteady instabilities are most likely to be detrimental (i.e., advancing the transition) within the context of BFM for the conditions of the present study.

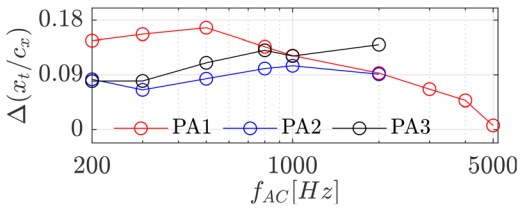

FIG. 5. Transition shift $\Delta(x_t/c_x)$ at $V_{p-p} = 10$ kV for various f_{AC}. The data points are plotted at $f_{AC} = 200$, 300, 500, 800, 1000, 2000, 3000, 4000, and 5000 Hz.

IV. PA EFFECT ON UNSTEADY PERTURBATIONS

In this section, a single hotwire probe is used to measure flow velocity in the boundary layer. To avoid dielectric layer and electrode degradation during the lengthy hotwire measurements, the PAs are operated in a limited range of parameters, namely, a single voltage amplitude of $V_{p-p} = 8$ kV and frequencies of $f_{AC} = 200$ and 3000 Hz. In order to assess the statistical properties of PA-induced disturbances, power spectral density (PSD), bandpass filtering, and spanwise-wavenumber spectra of the hotwire measurements are discussed in the following Secs. IV A-C.

A. Spectral characteristics of velocity fluctuations

As mentioned before, the inherent unsteadiness within the PA forcing is expected to induce unsteady disturbances in the boundary layer. Ultimately, the interaction between stationary and traveling CF instabilities as well as the secondary instability mechanism (associated with stationary CF vortices) can be affected, with repercussions on the final transition breakdown. Previous studies have shown that the underlying mean velocity gradient locations have a strong correlation with the developing types of CF instabilities.[5,10] For instance, the type III instability is associated with the local maximum spanwise gradient of the mean flow and typically develops in the inner side of the upwelling region of the CF vortex [region B outlined by the red dashed lines in Fig. 6(a)]. The *type I* secondary instability is strongly related to the local minimum spanwise gradient of the mean flow and emerges in the outer side of stationary vortices' upwelling region [region A outlined by the black dashed lines in Fig. 6(a)]. At similar conditions as in the present work, the type I mode features high frequencies (on the order of kHz), while the type III mode develops at low frequencies (on the order of Hz).[31] It follows that the CF instability types can be identified based on their corresponding dominant frequencies in combination with their localization within the underlying stationary vortex structure. As such, a PSD analysis is applied on the hotwire signal (for frequency information) where two monitoring points are defined based on local extrema of spanwise velocity gradient $\partial\bar{U}_{HW}/\partial\bar{z}$, namely, location-*a* and location-*b* as shown in Fig. 6(a). The PSD amplitude of the velocity fluctuation U'_{HW} is calculated by the average periodogram method[1] and non-dimensionalized as $\bar{P} = ((\Delta f/U_\infty^2)\text{PSD})^{1/2}$, where $\Delta f = 3.125$ Hz is the frequency resolution.

Figure 7 displays the non-dimensional spectra amplitude $\bar{P}$ at $x/c_x = 0.15$ under conditions of $f_{AC} = 200$ and 3000 Hz. Additionally, the amplitude $\bar{P}$ corresponding to a location outside the boundary layer (location-*r*) is plotted as a reference, indicating the far-field and freestream conditions. Generally, for $f_{AC} = 200$ Hz, the reference signals demonstrate a negligible level of electro-magnetic interference. Several discrete peaks of random high frequencies are only found for PA3. In contrast, weak electro-magnetic interference from the PA operation is observed for reference signals in cases of $f_{AC} = 3000$ Hz. Nonetheless, these undesired noise sources are assumed to have negligible influence on the measurement due to their relatively low amplitudes in comparison with PA-induced velocity fluctuations. An additional feature of the PSD is the low-power broad hump centralized around $f = 10$ kHz, which is related to the inherent characteristics of the hotwire bridge, thus not corresponding to physical events.[31]

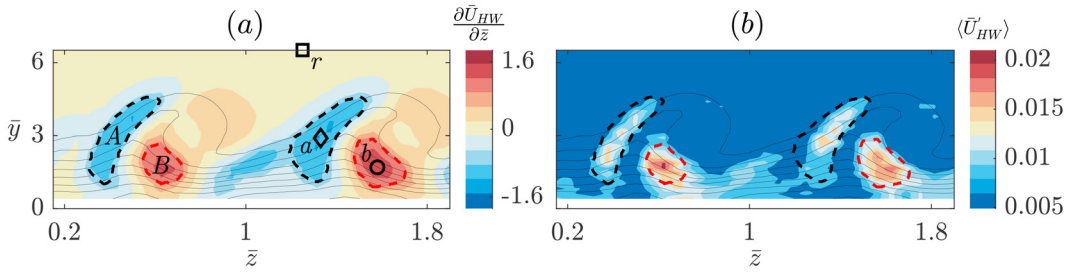

FIG. 6. (a) Spanwise gradient of mean velocity $\partial \bar{U}_{HW}/\partial \bar{z}$ and (b) non-dimensional velocity fluctuation amplitude $\langle \bar{U}'_{HW} \rangle$ for PA-off at $x/c_x = 0.2$. Location-*a* and location-*b* indicate the local peaks of velocity gradients. Location-*r* is used to monitor freestream conditions. Black and red dashed lines outline the minimum and maximum velocity spanwise gradient regions A and B, respectively.

As shown in Figs. 7(a) and 7(b), at both location-*a* and location-*b*, PA forcing at $f_{AC} = 200$ Hz evidently amplifies velocity fluctuations compared with PA-off. Specifically, strong spectral peaks are found at $f = 200$ Hz and higher superharmonics. At location-*b*, low-frequency velocity fluctuations ($f < 1000$ Hz) appear more amplified than high-frequency components, especially for PA1 which is located most upstream. On the other hand, fluctuations within a broad range of high frequencies ($f > 1000$ Hz) are evidently amplified at location-*a* by PA3. In cases of forcing at $f_{AC} = 3000$ Hz as shown in Figs. 7(c) and 7(d), the amplitudes $\bar{P}$ at both monitoring locations under PA-on further confirm the unsteady nature of plasma forcing. As shown in PA1 case at $f_{AC} = 3000$ Hz [Fig. 7(d)], low-frequency fluctuations (which are locally unstable as predicted by LST) are still enhanced at location-*b*, despite the high-frequency plasma excitation. The triggering of these low-frequency fluctuations has been previously observed by Serpieri *et al.*[8] where PAs operated at high f_{AC} as well. One possible source of these low-frequency fluctuations could be attributed to the stochastic processes of the inherent micro-discharge in the plasma formation, as identified by Moralev *et al.*[25] Moreover, this enhancing effect on low-frequency fluctuations (at location-*b*) shows a strong dependence on PA locations as it decreases from PA1 to PA3, which is similar to the trend observed at $f_{AC} = 200$ Hz. In contrast, high-frequency fluctuations are significantly amplified at location-*a* by the most downstream PA (i.e., PA3).

To identify the spatial localization of the various spectral signatures observed, the time series of velocity fluctuations are bandpass-filtered using digital fourth-order Butterworth filters. These filters feature a selected center frequency f_B with a narrow pass-bandwidth of

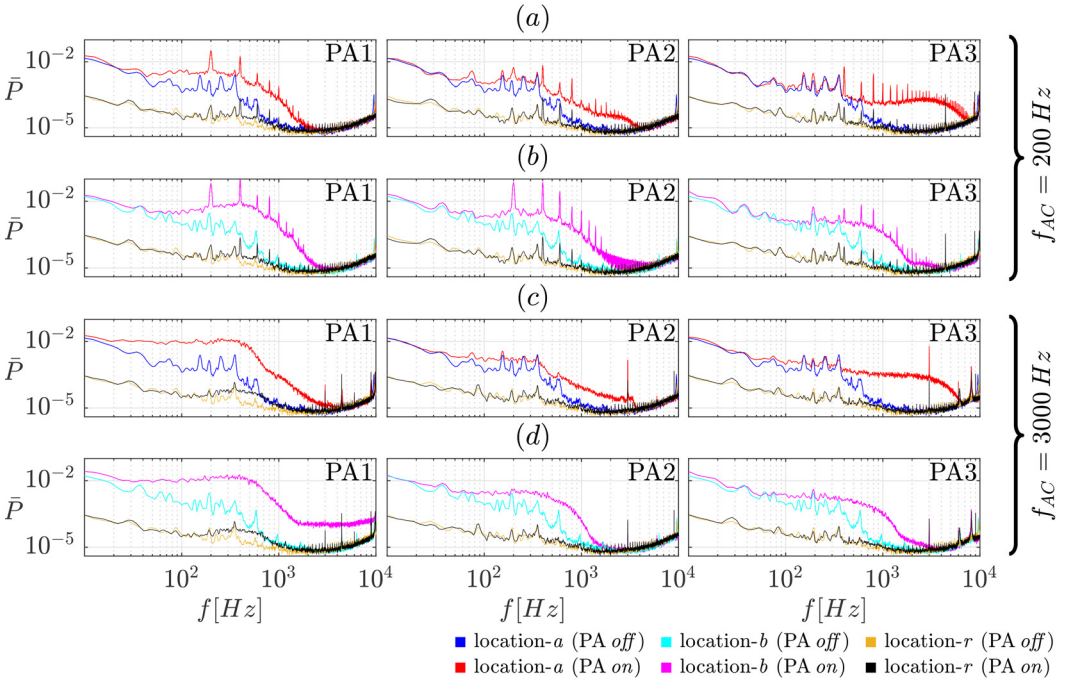

FIG. 7. Non-dimensional spectra $\bar{P}$ of velocity fluctuations at $x/c_x = 0.15$ for (a) location-*a*, $f_{AC} = 200$ Hz; (b) location-*b*, $f_{AC} = 200$ Hz; (c) location-*a*, $f_{AC} = 3000$ Hz; (d) location-*b*, $f_{AC} = 3000$ Hz.

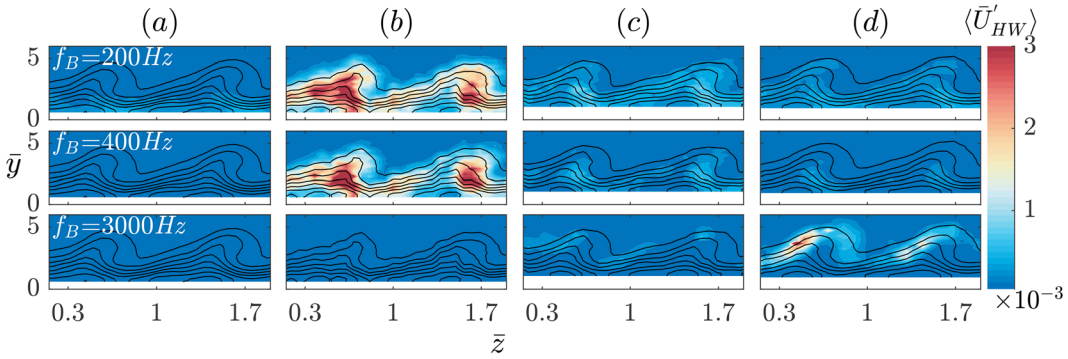

FIG. 8. Bandpass filtered velocity fluctuation fields $\langle \bar{U}'_{HW} \rangle$ for (a) PA-off; (b) PA1; (c) PA2; (d) PA3. All PAs are operating at $f_{AC} = 3000$ Hz ($V_{p-p} = 8$ kV), measurements at $x/c_x = 0.15$. The black iso-lines illustrate non-dimensional mean flow $\bar{U}_{HW}$ (20 levels from 0 to 0.85).

4 Hz. Representative frequency-filtered velocity fluctuations are illustrated in Fig. 8, corresponding to the $f_{AC} = 3000$ Hz case in Fig. 7. As expected, the unsteady fluctuations in PA-*off* cases have extremely low amplitudes and are significantly amplified at distinct frequencies by PA forcing depending on the PA location. Based on the frequencies and locations of these amplified fluctuations, two specific CF instabilities are recognized, namely, the type I and type III modes. In combination with the PSD results, the low-frequency fluctuations (200 Hz $< f <$ 800 Hz) centralized within region *B* are related to type III and the high-frequency fluctuations (2000 Hz $< f <$ 4000 Hz) centralized within region *A* are related to type I.

B. Amplitude and growth of velocity fluctuations

The identified types of CF instabilities are quantified in the following manner. Two spatial masks are defined as regions for which the underlying spanwise velocity gradient $\partial \bar{U}_{HW}/\partial \bar{z}$ exceeds a certain threshold. The mask for the PA-*off* case at $x/c_x = 0.2$ is given as an example in Fig. 6(a) with corresponding fluctuations in Fig. 6(b). Specifically, region *A* ($\partial \bar{U}_{HW}/\partial \bar{z} < -0.63$) is used to trace type I modes and region *B* ($\partial \bar{U}_{HW}/\partial \bar{z} > 0.94$) for type III modes. While the absolute value of these thresholds is chosen heuristically, the thresholds are kept constant for the entire parameter range, ensuring comparable outcomes. According to the PSD results, the velocity fluctuations are strongly amplified at the forcing frequency f_{AC} and its harmonics. As such, fluctuations at selected frequencies are quantified by adapting the bandpass filter frequency, namely, $f_B = 200$, 400, 600, and 800 Hz for the low-frequency type III modes and $f_B = 2000$, 2400, 3000, 3600, and 4000 Hz for the high-frequency type I modes. The non-dimensional amplitudes of frequency-filtered velocity fluctuations are spatially integrated in the mask regions following:

$$\bar{A}(f_B) = \frac{1}{s_t} \int\int_s \langle \bar{U}_{HW} \rangle \mathrm{d}s, \tag{2}$$

where s_t denotes the area of the corresponding region *A* or *B*. The non-dimensional amplitudes of velocity fluctuations at selected frequencies f_B are reported in Fig. 9. Specifically, integral amplitudes of type I and type III modes are distinguished by markers diamond and open circle, respectively. The PA-off case at $x/c_x = 0.2$ is chosen as a reference and shown in black color.

Figure 9(a) illustrates cases of $f_{AC} = 200$ Hz for all Pas. Unfortunately, the case of $x/c_x = 0.2$ is not recorded for PA1 due to actuator malfunction during the experiment. Instead, a supplementary measurement of PA1 at $x/c_x = 0.175$ is used for the following

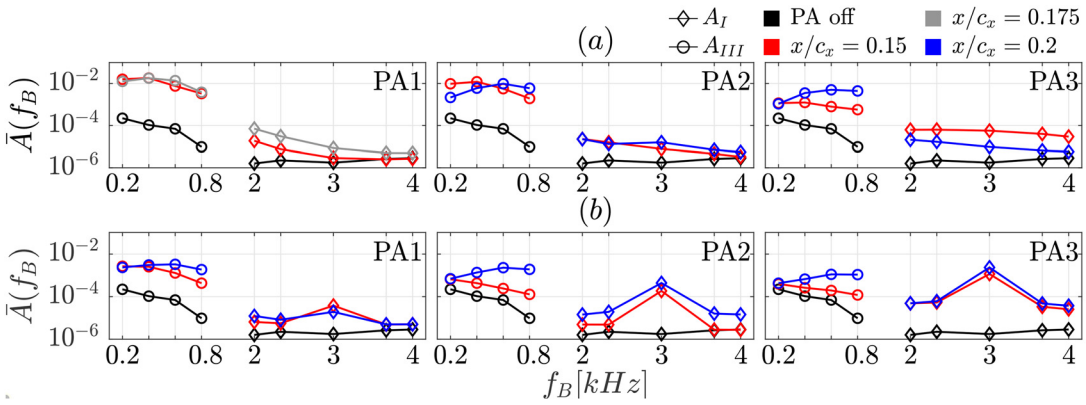

FIG. 9. Spatially integrated amplitude $\bar{A}(f_B)$ for type I and type III modes where PAs work at (a) $f_{AC} = 200$ Hz; (b) $f_{AC} = 3000$ Hz. The data points are plotted at $f_B = 200$, 400, 600, 800, 2000, 2400, 3000, 3600, and 4000 Hz.

discussion. The current results shed light on the effects of low forcing frequency $f_{AC} = 200$ Hz and PA location on the induced type I and type III modes. Inspecting the fluctuation amplitudes at $x/c_x = 0.15$, type III modes are found to be significantly amplified by Pas, compared with the reference. Moreover, the amplifying effect decreases from PA1 to PA3, agreeing well with the observed PSD. In contrast, type I modes are noticeably amplified by PA3 even though the forcing frequency is fixed at 200 Hz. Secondary instabilities of type-I are known to develop and amplify when the underlying stationary vortex has sufficiently modulated the boundary layer.[1] The PA3 is indeed located reasonably downstream, and as such, the present effect highlights the important role of PA location in inducing this type of disturbances.

As the flow develops downstream (i.e., $x/c_x = 0.2$), the type III modes generally amplify and reach comparable amplitudes for all tested Pas, despite their notably different amplitudes at $x/c_x = 0.15$. Moreover, it appears that, at $x/c_x = 0.2$, type III modes of higher harmonics are more amplified than those of primary forcing frequency. The origin of this effect is currently not clear, although the cascade of energy to higher harmonics might be indicative of non-linear interactions. The type I modes significantly amplified by PA3 at $x/c_x = 0.15$, rapidly decay at $x/c_x = 0.2$, for which the amplitudes remain as low as in cases of PA1 and PA2. The sudden attenuation contradicts the established behaviors of nominal type I instabilities, which, in unforced flows, experience a fast growth and lead to transition rapidly once stationary CF instabilities reach amplitude saturation. Nevertheless, in the current experiment, the amplitude of stationary CF vortices at $x/c_x = 0.2$ (defined as the maximum spanwise standard deviation of mean flow, $\langle \bar{U}_{HW} \rangle_z$) attains a value of 0.12 for PA3 (0.116 for the PA-off case). This is notably lower than the typical saturation amplitude (e.g., 0.21 by Serpieri and Kotsonis[31] and approximately 0.2 by Downs *et al.*[42]). As such, the unstable shear (which supports type I modes) appears not strong enough to sustain the growth of these high-frequency type I modes resulting in their eventual decay.

Figure 9(b) illustrates all PA cases for $f_{AC} = 3000$ Hz. Compared with PA-off, the low-frequency type III modes are evidently enhanced by the PA forcing despite the high f_{AC}. Specifically, these type III modes are most amplified by PA1. In contrast, an opposite tendency is observed for type I modes, which are significantly amplified by PA3 while only limitedly enhanced by PA1 (more evident at $x/c_x = 0.2$). Different from the observation of $f_{AC} = 200$ Hz, the type I modes induced by PA3 remain at high amplitudes, contributing significantly to the growth of CF instabilities. For each case, while there is an overall increase in amplitude of type I frequencies, the modes corresponding to the forcing frequency are particularly enhanced.

C. Spanwise-wavenumber spectra

As indicated by the LST results, primary unsteady structures in the swept wing boundary layer are essentially comprised of positive and/or negative traveling CF instabilities from the perspective of modal decomposition. Within the presently used coordinate system, the positive and negative modes propagate outboard $(+z)$ and inboard $(-z)$, respectively, in the yz plane [as shown in Fig. 3(a)]. The LST results in Sec. II E predict that these traveling pairs feature different growth rates for a given frequency and spanwise wavelength combination. Therefore, one can expect the negative and positive traveling modes to play different roles in the instability development and ultimately the ensuing transition. In this section, spanwise-wavenumber spectra are calculated, aiming at investigating the physical features and spatial organization of these traveling modes.

The deterministic conditioning of induced flow disturbances due to the PA unsteady forcing enables the phase-resolved analysis of the hotwire time series. Capitalizing on the synchronization between hotwire and PA voltage signals, the temporal velocity series are re-organized to align with a constant initial phase with respect to the voltage signal. Consequently, the re-organized velocity sequences are subjected to a two-dimensional FFT operation (in time and spanwise space z). The outcome provides a frequency-wavenumber spectrum at each y location.[43] In order to compare the traveling pairs, the amplitudes of the one-sided frequency-wavenumber spectra are extracted at desired frequencies (e.g., the forcing frequency and its harmonics). For consistency with established experimental and numerical studies, the double-spectral notation (h, k) is adopted to refer to generalized CF instability modes featuring integer multiples of the reference frequency f_0 and spanwise wavenumber γ_0, namely, $h = f/f_0$, where $f_0 = 200$ Hz and $k = \gamma/\gamma_0$, where $\gamma_0 = 1/\lambda_0$, $\lambda_0 = 8$ mm.

Figures 10(a)–10(c) illustrates representative spanwise-wavenumber spectra of low-frequency traveling modes for PA3 ($f_{AC} = 200$ Hz, $x/c_x = 0.2$), while Figs. 10(d)–10(f) shows the corresponding velocity fluctuation fields $\langle \bar{U}_{HW} \rangle$. Similar outcomes are found in cases of PA1 and PA2 and not shown here for brevity. The spanwise-wavenumber spectral amplitude is non-dimensionalized as $\bar{P}_z = (\Delta f \Delta\gamma / U_\infty)P$, where $\Delta f = 0.5$ Hz and $\Delta\gamma = 62.5\,\mathrm{m}^{-1}$ are the frequency and wavenumber resolution, respectively. The black dashed line represents the maximum spanwise standard deviation (mode shape) of the time-averaged velocity $\langle \bar{U}_{HW} \rangle_z$, indicating the approximate wall-normal location of the maximum amplitude of stationary CF vortices. As shown in Figs. 10(a)–10(c), for low-frequency modes of $(2, k)$, $(3, k)$, and $(4, k)$, significant spectral amplitudes are found in the vicinity of the maximum $\langle \bar{U}_{HW} \rangle_z$, showing that the wall-normal distribution of traveling modes strongly depends on the frequency, as observed by Casacuberta *et al.*[44] Compared with the negative traveling modes $(h, -k)$, positive traveling modes $(h, +k)$ are evidently more amplified by the PA forcing. The dominance of positive traveling modes is also experimentally observed by Borodulin *et al.*[45,46] and agrees well with previous LST predictions.

It must be noted here that the employed actuators are fabricated, installed, and operated in a nominally spanwise-invariant manner. As such, the actuators are expected to locally induce 2D modes, that is, $(h, 0)$. Notwithstanding, significant spectral amplitudes are found for traveling modes of $(h, \pm 1)$, which feature a spanwise wavelength corresponding to the DRE spacing. The appearance of these modes can be attributed to the non-linear interaction between the DRE-induced stationary mode (0, 1) and PA-induced unsteady modes $(h, 0)$. As a consequence, these low-frequency traveling modes (where positive traveling modes play a dominant role) interact with the stationary mode (0, 1) and result in type III modes, as confirmed by the corresponding $\langle \bar{U}_{HW} \rangle$ fields in Figs. 10(d)–10(f). Figure 11 illustrates the spanwise-wavenumber spectra and velocity fluctuation $\langle \bar{U}_{HW} \rangle$ of high-frequency modes for PA3 ($x/c_x = 0.15$). It should be noted that Figs. 11(c) and 11(f) are at the condition of $f_{AC} = 3000$ Hz, while the rest are at $f_{AC} = 200$ Hz. In contrast to low-frequency modes, considerable spectral amplitudes are found above the maximum $\langle \bar{U}_{HW} \rangle_z$ for

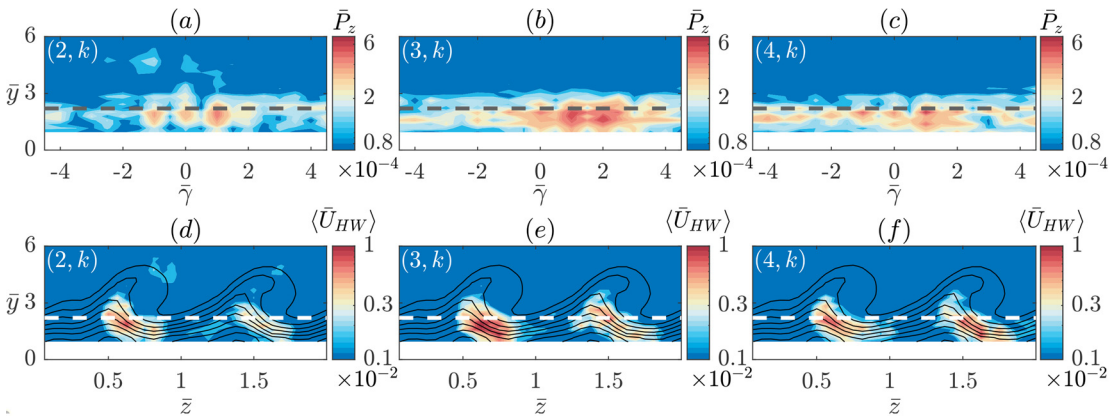

FIG. 10. (a)–(c) Spanwise-wavenumber spectra $\bar{P}_z$; (d)–(f) frequency-filtered fluctuation $\langle \bar{U}_{HW} \rangle$ for PA3 at $x/c_x = 0.2$ ($f_{AC} = 200$ Hz). Dashed line indicates the $\bar{y}$ location of the maximum $\langle \bar{U}_{HW} \rangle_z$.

high-frequency modes of $(10, k)$ and $(15, k)$. Moreover, in contrast to the trend found for low-frequency modes, negative traveling modes appear to be more amplified regarding the high-frequency modes.

To evaluate the PA effects on the negative and positive traveling modes, maximum spectral amplitudes and their corresponding wall-normal locations are quantified for cases at $x/c_x = 0.2$ (except PA1, which is measured at $x/c_x = 0.175$). For $f_{AC} = 200$ Hz, only low-frequency modes [i.e., $(1, k)$, $(2, k)$, $(3, k)$, and $(4, k)$] are considered since high-frequency modes feature negligible amplitudes at these conditions. In contrast, the high-frequency mode $(15, k)$ is extracted from cases of $f_{AC} = 3000$ Hz. The wall-normal location $\bar{y}_m$ and amplitude $\bar{P}_m$ where the negative and positive traveling modes attain a maximum are tracked within $-4 \le k \le -1$ and $+1 \le k \le +4$, respectively. The results are summarized in Fig. 12, where the marker diamond denotes negative traveling modes and the marker open circle indicates positive traveling modes. The black dashed line in Fig. 12(a) indicates the average $\bar{y}$ location of maximum $\langle \bar{U}_{HW} \rangle_z$ for all cases at $x/c_x = 0.2$.

As shown in Fig. 12(a), the low-frequency modes are located lower and closer to the maximum $\langle \bar{U}_{HW} \rangle_z$, while the high-frequency modes are distributed above the maximum $\langle \bar{U}_{HW} \rangle_z$, confirming the association with type III and type I instabilities, respectively. Nonetheless, no clear trend in $\bar{y}_m$ is found when these modes are distinguished by their traveling directions. Figures 12(b)–12(f) illustrate the amplitude $\bar{P}_m$ for the maximum positive and negative traveling modes. For cases at $f_{AC} = 200$ Hz, the positive traveling modes are generally more amplified than negative traveling modes for $(2, k)$, $(3, k)$, and $(4, k)$, though no clear trend is found for $(1, k)$. In contrast, negative traveling modes prevail among the high-frequency modes of $(15, k)$ for $f_{AC} = 3000$ Hz, agreeing well with the previous observation.

V. CONCLUSION

A. Effects of PA location and frequency

The present study experimentally inspects the effects of plasma actuator (PA) forcing in a swept wing boundary layer. More specifically, forcing frequency f_{AC} and forcing location of PAs are

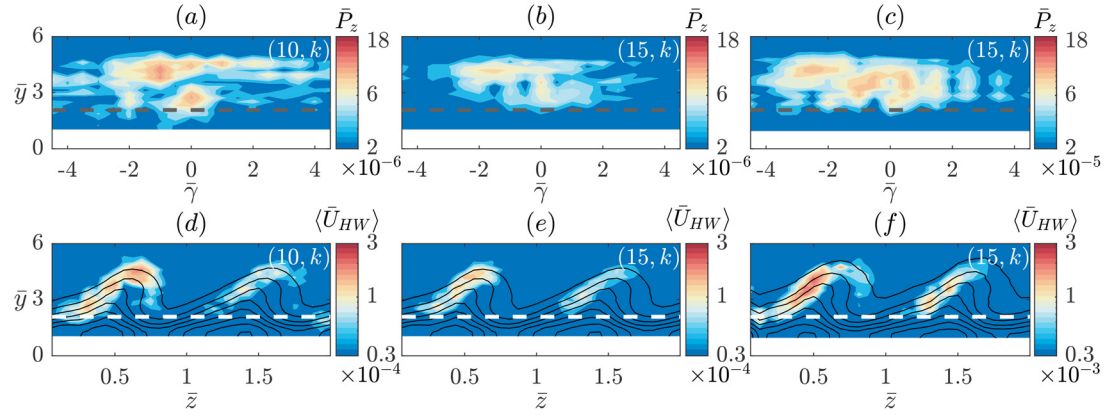

FIG. 11. (a)–(c) Spanwise-wavenumber spectra $\bar{P}_z$; (d)–(f) frequency-filtered fluctuation $\langle \bar{U}_{HW} \rangle$ for PA3 at $x/c_x = 0.15$. (c) and (f) are at $f_{AC} = 3000$ Hz, while the rest are at $f_{AC} = 200$ Hz. Dashed line indicates the $\bar{y}$ location of the maximum $\langle \bar{U}_{HW} \rangle_z$.

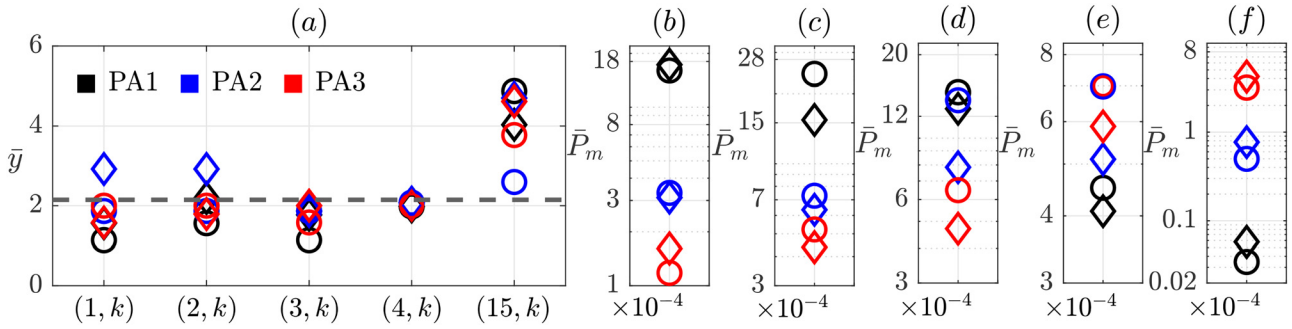

FIG. 12. (a) Wall-normal location $\bar{y}_m$; (b)–(f) Spectral amplitude $\bar{P}_m$ for traveling modes at $x/c_x = 0.2$ (except PA1 at $x/c_x = 0.175$). (b)–(f) correspond to $(1,k)$, $(2,k)$, $(3,k)$, $(4,k)$, and $(15,k)$ modes, respectively. The $(15,k)$ modes correspond to cases of $f_{AC} = 3000$ Hz and the rest to $f_{AC} = 200$ Hz. Diamond denotes negative traveling modes, while open circle denotes positive traveling modes.

investigated with respect to laminar–turbulent transition and instabilities development. Critical stationary CF vortices are conditioned using DREs to reproduce a critical scenario corresponding to realistic flight conditions. In agreement with LST results, the quantified transition locations demonstrate that low-frequency plasma forcing acts toward significant promotion of transition, particularly in regard to the most upstream forcing location (PA1). In contrast, the influence of low-frequency forcing is considerably weakened at more downstream forcing locations (PA2 and PA3). Considering that the boundary layer is unstable to traveling instability modes at all PA locations, the upstream introduction of low-frequency disturbances provides longer streamwise distance for spatial development, thus resulting in higher instability amplitude and earlier transition. This outcome further confirms the previous observations of Yadala *et al.*[24] and Serpieri.[8] Instead, although visibly altering the transition front topology, PA forcing at high frequencies appears to have an overall weaker effect on transition location.

The velocity fluctuations are further quantitatively investigated by hotwire scans at $x/c_x = 0.15$ and 0.2, respectively. Similar to previous experiments of Serpieri *et al.*[8] and Baranov *et al.*,[26] considerable spectral energy appears at low frequencies even when forcing is applied at high $f_{AC} = 3000$ Hz. This is attributed to the intrinsic unsteadiness in the discharge, similar to what was found in 2D boundary layers by Moralev *et al.*[25] The power spectral density and narrow bandpass filtering demonstrate the efficacy of the upstream PA forcing to enhance low-frequency type-III instabilities, while the downstream PA forcing appears to amplify high-frequency type-I instabilities.

The results highlight the strong dependence of PA-induced CF instabilities on f_{AC} and PA locations. In a boundary layer dominated by stationary CF vortices, it can be concluded that low-frequency type III instabilities are playing a dominant role for all PA locations when forcing is performed at low $f_{AC} = 200$ Hz. Though pronounced high-frequency type I instabilities are provoked by the downstream PAs, they consequently decay, possibly due to the insufficient strength of the flow shears produced by the still growing (i.e., not saturated) stationary CF vortices. In contrast, at high forcing frequency of f_{AC} to 3000 Hz, the effect on high-frequency type I instabilities is evidently pronounced. Ultimately, the strong sensitivity of the emerging type of unsteady disturbances appears to strongly correlate with the local receptivity of the boundary layer. At more upstream locations, the boundary layer is locally receptive and unstable to primary traveling modes, while at more downstream locations, to secondary high-frequency modes.

B. A comment on BFM efficacy

Reconciling previous studies of Yadala *et al.*,[24] Serpieri *et al.*,[8] and Peng *et al.*[41] as well as the current experiment, the stochastic PA-induced disturbances at both low and high frequencies can potentially damage the PA effectiveness for transition delay, at least within the context of BFM. For instance, to achieve the BFM control, the PA generally requires high power input and needs to be positioned close to the leading edge in order to favorably manipulate the CF component. As a consequence, the low-frequency disturbances could be initiated with high amplitudes and at extremely upstream locations. At these regimes, flow receptivity to type-III instabilities is high and can favor the growth of low-frequency CF instabilities thus weakening the BFM performance. Similarly, if the actuator is placed more downstream, then it inevitably operates in a region of heightened receptivity to type I instabilities, which are shown to be triggered by both high- and low-frequency PA forcing.

As such, minimizing unwanted unsteady disturbances introduced by PAs emerges as a key point toward improving BFM efficacy. Such effort needs to take into consideration of the complete stability and receptivity characteristics of the flow. The PA used in the current experiment is essentially tailored to produce a spanwise-invariant body force distribution. Possible unsteadiness in the body force can give rise to the (1, 0) mode as found in Figs. 10 and 11. Meanwhile, the stationary (0, 1) mode is enhanced in the present boundary layer due to the DRE conditioning, and in a possible application by general surface roughness. As a consequence, non-linear interactions between these two dominant modes result in the significant growth of traveling modes $(1, \pm 1)$. Following relevant numerical works of Guo and Kloker[13] and Dörr and Kloker,[21,22] the $(1, \pm 1)$ modes are unstable traveling modes featuring significant amplification in CF dominated boundary layers. Therefore, the wing surface roughness (either discrete or random) appears as a second key factor in BFM control.

Finally, the outcomes from the spanwise-wavenumber spectra inspire an alternative PA-based approach for the CF instability control. As illustrated, the typical type III instabilities are essentially dominated by the positive traveling modes. Therefore, tailored PA operation can be envisioned where the phase of the supplied voltage signal is

adjusted such to introduce negative traveling waves to directly compensate type III instabilities. However, such wave-cancelation technique needs sensors to detect the phase of traveling waves, which raises additional requirements for designing the control system for practical applications.

ACKNOWLEDGMENTS

K. Peng would like to appreciate the financial support of the China Scholarship Council (CSC). M. Kotsonis is supported by the European Research Council (ERC), through StG GLOWING (No. 803082). The authors would like to further acknowledge technical support from S. Bernardy and E. Langedijk during the experimental preparation. A dedicated acknowledgement goes to colleagues G. Zoppini, T. Michelis, and A. Rius-Vidales for their contributions and support.

AUTHOR DECLARATIONS

Conflict of Interest

The authors have no conflicts to disclose.

Author Contributions

Kaisheng Peng: Conceptualization (lead); Data curation (lead); Formal analysis (lead); Methodology (lead); Writing – original draft (lead). **Francesco Avallone:** Supervision (supporting); Writing – review & editing (equal). **Marios Kotsonis:** Conceptualization (equal); Methodology (equal); Supervision (equal); Writing – review & editing (lead).

DATA AVAILABILITY

The data that support the findings of this study are available from the corresponding author upon reasonable request.

REFERENCES

[1]E. B. White and W. S. Saric, "Secondary instability of crossflow vortices," J. Fluid Mech. **525**, 275 (2005).
[2]Z. Guo and M. J. Kloker, "Control of crossflow-vortex-induced transition by unsteady control vortices," J. Fluid Mech. **871**, 427–449 (2019).
[3]H. Bippes, "Basic experiments on transition in three-dimensional boundary layers dominated by crossflow instability," Prog. Aerosp. Sci. **35**, 363–412 (1999).
[4]W. S. Saric, H. L. Reed, and E. B. White, "Stability and transition of three-dimensional boundary layers," Annu. Rev. Fluid Mech. **35**, 413–440 (2003).
[5]M. R. Malik, F. Li, M. M. Choudhari, and C.-L. Chang, "Secondary instability of crossflow vortices and swept-wing boundary-layer transition," J. Fluid Mech. **399**, 85–115 (1999).
[6]R. D. Joslin, "Aircraft laminar flow control," Annu. Rev. Fluid Mech. **30**, 1–29 (1998).
[7]R. Messing and M. J. Kloker, "Investigation of suction for laminar flow control of three-dimensional boundary layers," J. Fluid Mech. **658**, 117 (2010).
[8]J. Serpieri, S. Y. Venkata, and M. Kotsonis, "Conditioning of cross-flow instability modes using dielectric barrier discharge plasma actuators," J. Fluid Mech. **833**, 164–205 (2017).
[9]W. Saric, R. Carrillo, Jr., and M. Reibert, "Leading-edge roughness as a transition control mechanism," in *36th AIAA Aerospace Sciences Meeting and Exhibit* (AIAA, 1998), p. 781.
[10]P. Wassermann and M. Kloker, "Mechanisms and passive control of crossflow-vortex-induced transition in a three-dimensional boundary layer," J. Fluid Mech. **456**, 49 (2002).
[11]S. M. Hosseini, D. Tempelmann, A. Hanifi, and D. S. Henningson, "Stabilization of a swept-wing boundary layer by distributed roughness elements," J. Fluid Mech. **718**, R1 (2013).
[12]W. S. Saric, D. E. West, M. W. Tufts, and H. L. Reed, "Experiments on discrete roughness element technology for swept-wing laminar flow control," AIAA J. **57**, 641–654 (2019).
[13]Z. Guo and M. J. Kloker, "Effects of low-frequency noise in crossflow transition control," AIAA J. **58**, 1068–1078 (2020).
[14]S. Yadala, M. T. Hehner, J. Serpieri, N. Benard, and M. Kotsonis, "Plasma-based forcing strategies for control of crossflow instabilities," AIAA J. **59**, 3406–3416 (2021).
[15]T. C. Corke, C. L. Enloe, and S. P. Wilkinson, "Dielectric barrier discharge plasma actuators for flow control," Annu. Rev. Fluid Mech. **42**, 505–529 (2010).
[16]N. Benard and E. Moreau, "Electrical and mechanical characteristics of surface ac dielectric barrier discharge plasma actuators applied to airflow control," Exp. Fluids **55**, 1846 (2014).
[17]M. Kotsonis, "Diagnostics for characterisation of plasma actuators," Meas. Sci. Technol. **26**, 092001 (2015).
[18]J. Kriegseis, B. Simon, and S. Grundmann, "Towards in-flight applications? A review on dielectric barrier discharge-based boundary-layer control," Appl. Mech. Rev. **68**, 020802 (2016).
[19]H. Tol, C. D. Visser, and M. Kotsonis, "Experimental model-based estimation and control of natural Tollmien–Schlichting waves," AIAA J. **57**, 2344–2355 (2019).
[20]S. Grundmann and C. Tropea, "Active cancellation of artificially introduced Tollmien–Schlichting waves using plasma actuators," Exp. Fluids **44**, 795–806 (2008).
[21]P. C. Dörr and M. J. Kloker, "Crossflow transition control by upstream flow deformation using plasma actuators," J. Appl. Phys. **121**, 063303 (2017).
[22]P. Dörr and M. Kloker, "Transition control in a three-dimensional boundary layer by direct attenuation of nonlinear crossflow vortices using plasma actuators," Int. J. Heat Fluid Flow **61**, 449–465 (2016).
[23]P. Dörr and M. Kloker, "Stabilisation of a three-dimensional boundary layer by base-flow manipulation using plasma actuators," J. Phys. D **48**, 285205 (2015).
[24]S. Yadala, M. T. Hehner, J. Serpieri, N. Benard, P. C. Dörr, M. J. Kloker, and M. Kotsonis, "Experimental control of swept-wing transition through base-flow modification by plasma actuators," J. Fluid Mech. **844**, R2 (2018).
[25]I. Moralev, I. Selivonin, and M. Ustinov, "On the stochastic forcing of the boundary layer by plasma actuators," Exp. Fluids **60**, 177 (2019).
[26]S. A. Baranov, S. L. Chernyshev, V. Y. Khomich, A. P. Kiselev, A. P. Kuryachii, S. I. Moshkunov, I. E. Rebrov, D. S. Sboev, S. N. Tolkachev, and V. A. Yamshchikov, "Experimental cross-flow control in a 3D boundary layer by multi-discharge plasma actuators," Aerosp. Sci. Technol. **112**, 106643 (2021).
[27]J. Arkesteijn, "Cross-flow instability control through base-flow modification using AC-DBD plasma actuators: An experimental investigation," Master thesis (Delft University of Technology, 2021).
[28]T. Corke, A. Arndt, E. Matlis, and M. Semper, "Control of stationary cross-flow modes in a Mach 6 boundary layer using patterned roughness," J. Fluid Mech. **856**, 822–849 (2018).
[29]A. Arndt, T. Corke, E. Matlis, and M. Semper, "Controlled stationary/travelling cross-flow mode interaction in a Mach 6.0 boundary layer," J. Fluid Mech. **887**, A30 (2020).
[30]G. Bonfigli and M. Kloker, "Secondary instability of crossflow vortices: Validation of the stability theory by direct numerical simulation," J. Fluid Mech. **583**, 229 (2007).
[31]J. Serpieri and M. Kotsonis, "Three-dimensional organisation of primary and secondary crossflow instability," J. Fluid Mech. **799**, 200–245 (2016).
[32]J. Serpieri and M. Kotsonis, "Design of a swept wing wind tunnel model for study of cross-flow instability," in *33rd AIAA Applied Aerodynamics Conference* (AIAA, 2015), p. 2576.
[33]G. Zoppini, S. Westerbeek, D. Ragni, and M. Kotsonis, "Receptivity of cross-flow instability to discrete roughness amplitude and location," J. Fluid Mech. **939**, A33 (2022).
[34]A. F. Rius-Vidales and M. Kotsonis, "Influence of a forward-facing step surface irregularity on swept wing transition," AIAA J. **58**, 5243–5253 (2020).
[35]M. Raffel, C. B. Merz, T. Schwermer, and K. Richter, "Differential infrared thermography for boundary layer transition detection on pitching rotor blade models," Exp. Fluids **56**, 30 (2015).

[36]A. F. Rius-Vidales, M. Kotsonis, A. P. Antunes, and R. Cosin, "Effect of two-dimensional surface irregularities on swept wing transition: forward facing steps," in *Fluid Dynamics Conference* (AIAA AVIATION Forum, 2018), p. 3075.
[37]J. Serpieri and M. Kotsonis, "Conditioning of unsteady cross-flow instability modes using dielectric barrier discharge plasma actuators," Exp. Therm. Fluid Sci. **93**, 305–318 (2018).
[38]G. Bonfigli, M. Kloker, and S. Wagner, "3-D-boundary-layer transition induced by superposed steady and traveling crossflow vortices," in *High Performance Computing in Science and Engineering* (Springer, 2003), pp. 255–271.
[39]L. M. Mack, "Boundary-layer linear stability theory," Special Course on Stability and Transition of Laminar Flow, AGARD Report No. 709 (3-1 to 3-81). (Jet Propulsion Laboratory, California Institute of Technology, Pasadena, CA, 1984).
[40]G. Bonfigli and M. Kloker, "Numerical investigation of transition caused by superposed steady and travelling crossflow vortices," Report No. IAG-TR-2005-CFTRANS (Institute of Aerodynamics and Gas Dynamics, University of Stuttgart, 2005).
[41]K. Peng, J. Arkesteijn, F. Avallone, and M. Kotsonis, "Experimental base flow modification on a swept wing using plasma forcing," Phys. Fluids **34**, 103614 (2022).
[42]R. S. Downs and E. B. White, "Free-stream turbulence and the development of cross-flow disturbances," J. Fluid Mech. **735**, 347–380 (2013).
[43]V. Borodulin, A. Ivanov, Y. Kachanov, and A. Roschektayev, "Distributed vortex receptivity of a swept-wing boundary layer: Part 1—Efficient excitation of CF modes," J. Fluid Mech. **908**, A14 (2021).
[44]J. Casacuberta, K. J. Groot, S. Hickel, and M. Kotsonis, "Secondary instabilities in swept-wing boundary layers: Direct numerical simulations and biglobal stability analysis," in *AIAA SCITECH 2022 Forum* (AIAA, 2022), p. 2330.
[45]V. Borodulin, A. Ivanov, Y. Kachanov, and D. Mischenko, "Experimental investigation of characteristics of steady and unsteady crossflow-instability modes developing in a 35-degree swept-airfoil boundary layer," in Proceedings of 17th International Conference Methods of Aerophysical Research (2014).
[46]V. Borodulin, A. Ivanov, Y. Kachanov, and A. Roschektaev, "Receptivity coefficients at excitation of cross-flow waves due to scattering of free-stream vortices on surface vibrations," J. Fluid Mech. **793**, 162–208 (2016).